Elucidating the Role of Chalcogenide-Based Interface Passivators in Enhancing the Stability of Perovskite Solar Cells

*Anupam Sadhu, Yuanyuan Guo, Teddy Salim, Qingde Sun, Subodh G. Mhaisalkar, Tze Chien Sum, Lydia H. Wong**

Mr. Anupam Sadhu, Dr. Teddy Salim, Dr. Qingde Sun, Prof. Subodh G. Mhaisalkar, Prof. Lydia H. Wong

School of Material Science and Engineering

Nanyang Technological University

Singapore 639798 Singapore

Email: LydiaWong@ntu.edu.sg

Mr. Anupam Sadhu, Prof. Subodh G. Mhaisalkar, Prof. Lydia H. Wong

Campus for Research Excellence and Technological Enterprise (CREATE)

Singapore 138602 Singapore

Prof. Subodh G. Mhaisalkar, Prof. Lydia H. Wong

Energy Research Institute @ NTU (ERI@N)

50, Nanyang Drive, Nanyang Technological University

Singapore 637553 Singapore

Dr. Yuanyuan Guo, Prof. Tze Chien Sum,

Division of Physics and Applied Physics, School of Physical and Mathematical Sciences

21 Nanyang Link, Nanyang Technological University

Singapore 637371, Singapore.

Keywords: Interface passivation, chalcogenide, defect passivation, perovskite solar cells

Abstract:

Chalcogenide-based Lewis bases are widely used in perovskite solar cells (PSCs) due to their effectiveness in passivating Pb^{2+} and Pb^{0}-related defects. However, the underlying principles governing their defect passivation and the relative efficacy of different chalcogen elements remain poorly understood. This study evaluates the effectiveness of oxygen, sulfur, and selenium-based interface passivator molecules in enhancing the stability and power conversion efficiency (PCE) of perovskite solar cell devices. The hard and soft acid and base (HSAB) principle has been utilized here to gain insights into the defect passivation behavior of chalcogenide-based molecules. The photoluminescence, ideality factor, and trap density measurements reveal that the sulfide and selenide-passivated devices exhibit superior defect passivation compared to the oxide-passivated control device. In terms of stability, the average T_{75} lifetime (time at which 75% of the initial PCE is retained) of the oxide, sulfide, and selenide passivated samples is 6%, 30%, and 50% higher compared to their un-passivated counterparts. This enhanced stability with the sulfide and selenide-based passivators can be attributed to their soft Lewis base nature, which resulted in stronger interaction with the Pb-related defects, as evidenced by the density-functional theory calculations and X-Ray photoelectron spectroscopy study.

1. Introduction:

Over the last decade, the rapid emergence of perovskite solar cells (PSC) has revolutionized the field of solar cells. Recently a world record power conversion efficiency (PCE) of 26.1% has been reported for PSC, which is equivalent to the record PCE of single-junction silicon solar cells (26.1%).[1] The remarkably high PCE of PSCs can be attributed to their unique properties, including exceptional defect tolerance, high absorption coefficient, low exciton binding energy, and tunable band gap.[2] However, the poor operational stability of perovskite solar cells has been the Achilles heel among its otherwise exceptional properties.

Due to the soft nature of the perovskite lattice, different environmental factors, like moisture, oxygen, heat, and light, can easily interact with the constituents in the lattice structure, leading to lattice distortion, phase decomposition, and ultimately the degeneration of the film.[3] While deep defects are the primary concern due to their ability to facilitate nonradiative recombination, they are relatively limited in the perovskite lattice because of their defect-tolerant nature.[4] On the other hand, polycrystalline perovskite films are generally filled with shallow defects owing to their low formation energy.[5] Although these shallow defects are believed to have an insignificant impact on the power conversion efficiency (PCE) of the perovskite solar cell (PSC), they can compromise stability by mediating various degradation reactions.[6] Thus, passivating both deep and shallow defects is crucial for enhancing the performance of the perovskite solar cell.

Various families of molecules, including Lewis acids, Lewis bases, and Zwitterions, have been studied for their ability to passivate different types of defects within the perovskite lattice.[7] Lewis base-based passivators have been widely used to passivate Pb^{2+} (V_I) and Pb^0-related defects due to their electron donor capabilities. Several chalcogenide-based groups, including -O, -S, -SO_4, have been found to be effective Lewis base defect passivators. However, despite

extensive investigation, the principles for designing effective defect passivators remain poorly understood. Some of the reports suggest that compared to oxygen, sulfide-based compounds have a superior ability to form adduct with the Pb atom due to their higher softness.[8] Nonetheless, the relative effects of sulfide and oxide-based passivators on the stability of perovskite solar cells are not yet fully comprehended. In addition, despite their exceptional Lewis base properties, selenium-based compounds have seldom been employed for defect passivation in perovskite solar cells.

In this study, we aim to understand the relative passivation strength of different chalcogenide-based Lewis bases from the standpoint of the hard and soft acid and base (HSAB) principle.[9] The HSAB theory has been widely employed for predicting the interaction strength between different Lewis acids and bases. This theory classifies Lewis acids and bases into three categories: soft, hard, and borderline, based on their properties, such as electronegativity, polarizability, charge-to-radius ratios, and size of ions and groups. According to this theory, soft acids interact strongly with soft bases, and hard acids interact strongly with hard bases, while the cross interactions between soft and hard compounds are relatively weak.[9-10]

The HSAB principles can be utilized to determine the softness and hardness of defects inside the perovskite lattice, which can subsequently be used to identify suitable passivators. Literature suggests that due to the larger ionic radius, low charge density, and filled outer orbitals, Pb^{2+} and Pb^{0} behave like soft (or borderline-soft) Lewis acids (Pb^{0} is softer than Pb^{2+}).[7a, 11] On the other hand, among the chalcogens (group 16 of the periodic table), the softness of the bases increases with atomic number. A more specific study has revealed that the interaction sequence of the chalcogenide elements with Pb^{2+} is in the following order: Se ≥ S >> O.[11a, 12] Based on these understandings, a hypothesis can be made that the sulfide and selenide compounds exhibit a stronger interaction with Pb^{2+} and Pb^{0} as compared to their oxide counterparts.

In this work, organophosphorus compounds with different chalcogen groups, namely triphenylphosphine oxide (TPPO), triphenylphosphine sulfide (TPPS), triphenylphosphine selenide (TPPSe), are used as interface passivators to compare the defect passivation effect of oxygen, sulfur, and selenium in the perovskite solar cells. The chosen molecules have similar structures, allowing us to directly attribute any differences in device performance to the basicity and softness of the chalcogenide atom. To our knowledge, this is the first report to compare the defect passivation and stability-enhancing ability of the three chalcogenide atoms in the context of a perovskite solar cell. Our findings show that all three interface passivators improved the power conversion efficiency (PCE) of the device to a similar extent compared to the control one. However, in terms of stability, the TPPS and TPPSe passivated devices were significantly superior to the control and TPPO passivated ones. The enhanced stability observed with the TPPS and TPPSe passivation can be attributed to their stronger interaction with the Pb^{2+} and Pb^{0} ions, which enables them to passivate a broader range of defects and maintain the dative bonds even in the presence of external stressors.

2. Results and discussions:

To evaluate the coordination ability of TPPO, TPPS, and TPPSe with the interfacial perovskite defects, density-functional theory (DFT) calculations were carried out. Figure 1.a and 1.b depict the simulated charge densities of two systems: (a) the pristine PbI_2-terminated (001) surface of α-$FAPbI_3$, and (b) the Lewis base molecule integrated onto the PbI_2-terminated (001) surface of the cubic α-$FAPbI_3$. α-$FAPbI_3$ composition was chosen because of its relatively simple structure and close resemblance to the composition used in this work's experimental part.[13] PbI_2 terminated (001) surface was selected due to its high stability and lower surface energy in $MAPbI_3$ and α-$FAPbI_3$ systems.[14] Additionally, since our Lewis base molecules are

designed to interact with the under-coordinated Pb sites, a study on the PbI_2 terminated surface yields more meaningful results. The interface passivators such as TPPX (X=O, S, Se) interacts with the under-coordinated Pb atoms through coordinate covalent bond as shown in Figure 1.b. To quantify the strength of these Lewis acid-base interactions, we calculated the binding energy of these organic molecules with the perovskite surface. The binding energy (E_b) is defined as ($E_b = E_{(P+S)} - E_S - E_P$), where $E_{(P+S)}$, E_S, and E_P represent the total energies of the binding system, the clean surface, and the passivator (TPPO, TPPS, and TPPSe), respectively. The binding energies for Pb-O (TPPO), Pb-S (TPPS), and Pb-Se (TPPSe) bonds were determined to be 2.9 eV, 3.51 eV, and 3.77 eV, respectively (Figure 1.c and Table S.1).[13] The higher binding energy for sulfur and selenium compared to oxygen is probably due to their better softness matching with Pb. According to this calculation, selenium-based passivators could potentially be more effective at passivating positively charged Pb-based defects compared to their sulfur-based counterparts.

As part of our evaluations, we also calculated the changes to the Fermi energy (E_F) to valence band maximum (VBM) distance (E_F-VBM) caused by the Pb-X interactions in the perovskite film (Figure 1.d). Passivated perovskite films showed markedly shifted (E_F-VBM) due to these interactions. It can be seen that the TPPSe passivated perovskite shows the most significant amount of shift in the VBM position, followed by TPPS and TPPO passivated perovskite films. The higher valance to Fermi distance in the TPPS and TPPSe systems indicate an increased electron/hole ratio in the perovskite film due to the transfer of higher electron density (from the passivator) into the perovskite film.

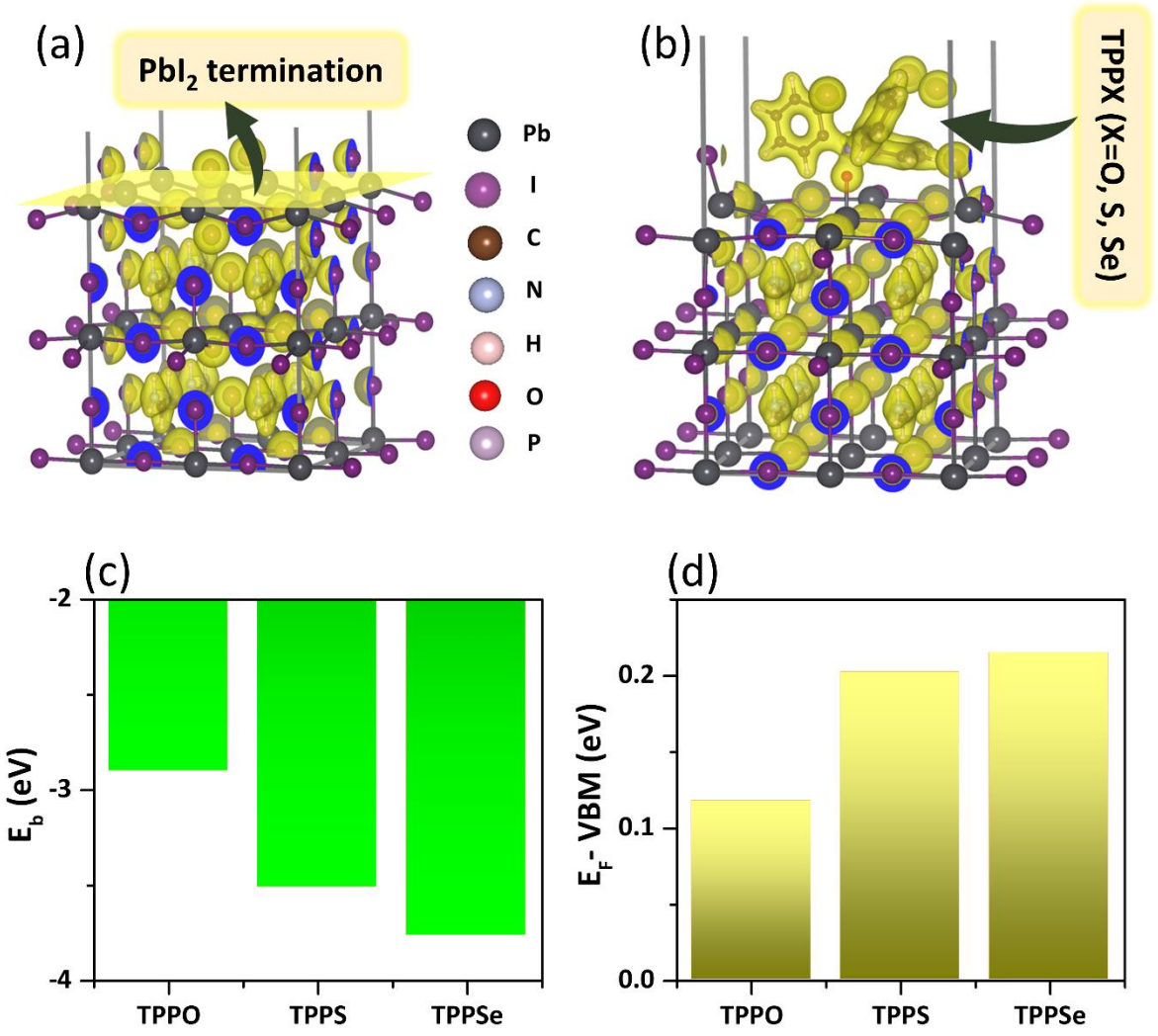

Figure 1. (a) Charge Density of PbI_2-terminated α-$FAPbI_3$ (001) supercell surface, (b) TPPX (X=O, S, Se) binding to the (001) surface of α-$FAPbI_3$. (c) Binding energy of TTPO, TPPS, and TPPSe binding to the PbI_2-terminated α-$FAPbI_3$ (001) surface. The observed decrease in binding energy in the order of TPPO, TPPS, and TPPSe indicates that TPPSe exhibits the highest binding affinity with $FAPbI_3$, demonstrating its superior binding capability. (d) The energy difference between the Fermi level and valence band maximum (VBM) in the three passivated systems.

An inverted architecture perovskite solar cell (Figure 2.a, 2.b) consisting of FTO/ NiO/ perovskite/ PCBM/ BCP/ Ag was used in this work. A triple cation perovskite with $Cs_{0.05}(MA_{0.17}FA_{0.83})_{0.95}Pb(I_{0.83}Br_{0.17})_3$ was employed for the absorber layer. The interface defect passivation layer consisting of organophosphorus molecules (TPPO, TPPS, and TPPSe)

was deposited on top of the NiO hole transport layer (HTL) using the spin coating method. For optimizing the thickness of the passivation layer, organophosphorus solutions of different concentrations ranging from 0.05 mg/ml to 2 mg/ml were used for the spin coating. As can be observed from Figure S.2, the highest PCEs for TPPO, TPPS, and TPPSe passivated devices were obtained at 0.25, 0.25, and 0.1 mg/ ml concentrations, respectively. Here onwards, these concentrations are used for further characterizations unless mentioned otherwise.

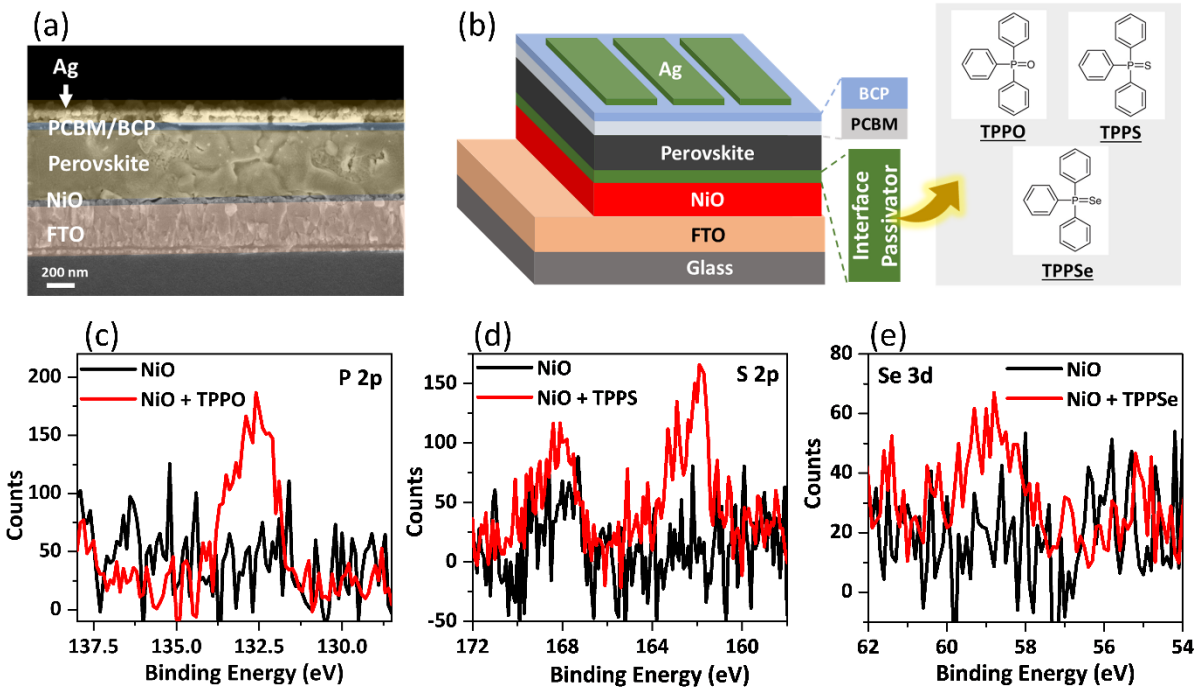

Figure 2. (a) Cross-section SEM of the inverted architecture perovskite solar cell used in this work (b) Device structure and the molecular structures of the passivating molecules used in this work. (c) P 2p (d) S 2p (e) Se 3d spectra from the XPS of TPPO, TPPS, and TPPSe coated NiO films, respectively, the XPS spectra are compared to the pristine NiO film.

Due to the small thickness, the passivation layers cannot be detected in the SEM cross-section of the devices. Therefore, XPS of the NiO surface with the passivation molecules (of optimized concentration) is performed to confirm the presence of the passivation molecules. P 2p spectra are used to verify the existence of TPPO. As can be observed from Figure 2.c, the pristine NiO

film is devoid of any P 2p peak, whereas, in the TPPO-coated one, a weak P 2p peak is visible, confirming the presence of the TPPO molecule at the NiO surface. Similarly, the presence of TPPS and TPPSe are confirmed using the S 2p and Se 3d peaks (Figure 2.d and 2.e). The relatively weak intensity of the Se 3d peak is due to the lower concentration of TPPSe used in this work. Figure S.3 shows the Ni 2p peaks in the presence of different interface passivators. In the presence of TPPO, Ni^{2+} and Ni^{3+} peak shows the maximum amount of shift, whereas TPPS and TPPSe cause a significantly lower amount of peak shift. These chemical interactions at the NiO surface might be able to passivate some of the trap states in the NiO surface.[15] The strength of the chemical interaction of the passivator with the target species is often associated with its defect passivation efficacy.[16] TPPO passivation, despite its strongest interactions (highest peak shift) with the NiO surface, does not lead to the best overall device improvements, as shown later. On the other hand, TPPS, which has a significantly weaker interaction with the NiO surface, yields the best overall device performance (stability and PCE). These correlations suggest that, though NiO surface trap passivation might have some impact on the device PCE, it is not the primary factor determining the device performance in this study. However, a more detailed study is needed to fully comprehend the nature and role of these chemical interactions. The impact of the passivation molecules on the valence band maximum (VBM) position of the NiO is also examined (Figure S.4). It is observed that the VBM of the NiO film undergoes a slight downward shift with the coating of the passivation layers. The highest shift is observed for the TPPSe-coated films, followed by the TPPS and TPPO passivated films. The slight change in the VBM position can improve the energy alignment with perovskite and thus facilitating better interfacial charge transfer to a certain degree.

At higher solution concentrations, the device performance of the TPPSe passivated devices drops more dramatically compared to TPPO and TPPS passivated ones (Figure S.2). To

understand if the compromised PCE is due to an intrinsic property of TPPSe or is a result of an undesirable reaction between the passivation molecule and NiO, passivation layers of increased thickness are deposited on NiO using solution concentrations of 2 mg/ml. The higher concentration is used to amplify the effect and facilitate better detection of any potential reaction between the passivation molecule and NiO. The film is heated to 105 °C for 30 min to replicate the perovskite annealing condition and then cleaned with IPA multiple times to remove any residual organic compounds (so that the effect is only from the product of reactions).

Table S.2 demonstrates that for TPPO and TPPS, the Ni^{2+} 2p peak shifts slightly towards lower binding energy, which may be due to the transfer of some lone pair electrons from residual sulfur atoms to Ni^{2+} through Lewis acid-base interactions (Figure S.5). However, with TPPSe treatment, the Ni^{2+} peak shows a notable shift towards higher binding energy. Moreover, Table S.3 shows a slight reduction in the oxygen vacancy peak area with TPPSe treatment (Figure S.6). The combination of both these factors indicates that TPPSe reacted with the undercoordinated Ni ions (therefore filling the V_O sites) to form Ni-Se-based secondary phase in the NiO surface. On the other hand, the TPPS and TPPO show no such reaction with the NiO film. This conclusion is further bolstered by the change in the absorption spectra of the NiO-TPPSe film after annealing, as shown in Figure S.7 (details in figure caption). The secondary phase in the perovskite-NiO interface for the TPPSe sample can cause carrier recombination and a charge transfer barrier in the interface. It is possible that at concentrations >0.1 mg/ml, the adverse effects of the TPPSe-NiO reaction outweigh the positive impacts of the passivation, causing a reduction in the device PCE.

To check if the passivator molecules in the NiO surface causes parasitic absorption, the transparency of the NiO film with and without the passivator molecules was measured (optimized concentration was used). As illustrated in Figure S.8.a, transparency changes were

negligible irrespective of the presence/absence of passivator molecules. The conductivity of the NiO film was also measured with and without the passivator molecules. As can be seen from Figure S.8.b, very little change in the conductivity of the NiO is observed after the coating of the passivator molecules. Although the TPPS sample showed slightly lower conductivity than the other three samples, its actual conductivity falls within the proximity of the standard deviation of conductivity shown by pristine NiO films. Therefore, it can be concluded that the coating of these interface passivators does not cause any meaningful change in the conductivity of the NiO film.

To investigate potential interactions between chalcogenide and lead atoms, X-ray photoelectron spectroscopy (XPS) was performed on 60 nm thick perovskite films with various passivators. Gas cluster Ar ion sputtering was performed to probe an area closer to the perovskite/NiO interface (*bulk*). Though the majority of the passivator molecules are expected to stay at the bottom interface through surface adsorption, some of the molecules might travel to the bulk of the perovskite film due to their finite solubility in the perovskite precursor solution.[17] The *bulk* data was collected near the bottom interface, the estimated location is 10-30 nm from the bottom interface. Figure S.9 and S.10 shows the Pb $4f_{7/2}$ (Pb^{2+}) spectra from the *surface* and *bulk* of perovskite films, both with and without the passivation layers. The passivated film's spectra show a noticeable shift towards lower binding energy in comparison to the control (Table S.4). This shift is due to the Lewis acid-base interaction between Pb^{2+} and the chalcogenide atoms, whereby some electron cloud gets transferred to Pb from the chalcogenide atom. Additionally, we found that the shifts for the Pb^{2+} peak in the *bulk* of the passivated films were more significant than at the *surface* (Figure S.10 and Table S.4). This difference is potentially due to the higher passivator concentration and stronger interaction between the perovskite and passivator near the bottom interface. The observed difference in peak shift between the surface and bulk of the perovskite indicates that passivator molecules

are primarily localized near the bottom interface. This interaction of the chalcogenide atoms with the Pb^{2+} ions will lead to the passivation of the interfacial Pb dangling bond and other charged Pb-related interfacial defects.[18] No significant difference is observed when comparing the core-level shifts among the three passivation molecules at both locations.

Pb^0-related defects have a significant adverse effect on the recombination behavior and degradation of the devices.[19] The binding energy of the Pb^0-related Pb $4f_{7/2}$ peak is also analyzed to understand the impact of the interface passivators on these defects (Figure 3.a). The Ar etching process produced a significant amount of Pb^0 species in the perovskite film due to a relatively faster etching rate of iodine (compared to Pb). These newly formed Pb^0 ions are not expected to bind to the interface passivators. Therefore, the Pb^0 peak from the *bulk* cannot be used for our analysis. Hence, only the *surface* XPS of the Pb^0 4f peak is analyzed.

It is observed that the passivation-induced peak shift is more substantial for the surface Pb^0 peaks than for the Pb^{2+} for all three passivators (Table S.4). This difference in the degree of peak shift is most likely due to the higher softness of the Pb^0 as compared to Pb^{2+} (softness of the Lewis acid increases with the reduction in the oxidation state), which leads to a stronger acid-base interaction.[12b] It is also observed that the TPPS passivation induces the most significant shift in the Pb^0 peak compared to the passivation with TPPO and TPPSe. For passivator with comparable thicknesses, the more significant shift for TPPS indicates a stronger interaction with Pb^0 than TPPO, which can be associated with the higher softness of TPPS (compared to TPPO) in the HSAB scale. On the other hand, despite a much lower concentration, TPPSe shows an almost equal peak shift to TPPO, indicating its much higher interaction strength due to its higher softness. The interaction (peak shift) sequence in Figure S.10 between the passivation molecules and $\mathbf{Pb^{2+}}$ $4f_{7/2}$ is expected to be similar. However, it is undetectable due to poor resolution caused by low passivator concentrations. The shift in the Pb 4f peak observed in the XPS study is consistent with our DFT results.

To further verify the interaction between the Pb and the passivation molecules, FTIR characterization is performed on a series of films prepared from the mixture of the organic passivator molecule and PbI_2. The use of PbI_2 instead of lead-based hybrid perovskite eliminates the effect of the methylammonium (MA^+) and formamidinium (FA^+) cations on the FTIR spectra of the passivator molecule, which allows for the observation of the impact of Pb-X interaction (X= O, S, Se) more clearly. As shown in Figure S.11, peaks related to the P=O, P=S, P=Se stretching vibration shift from 1186, 709 & 557 cm^{-1} to 1183, 713 & 559 cm^{-1} respectively, with the addition of the PbI_2 in the film.[20] This shift in the vibrational frequency is evidence of the charge delocalization due to the interaction with PbI_2.[21] However, due to the difference in the strength and characteristics among P=O, P=S, and P=Se bonds, it is challenging to substantiate any quantitative claim regarding the relative strength of the interactions.

Figure 3.b, 3.c show the UPS spectra of the *perovskite films* with and without the passivation layers. The work function (SECO, Figure 3.b), with respect to the vacuum, does not change after the incorporation of any of the passivation layers. However, the Fermi-to-valence distance (valence edge graph, Figure 3.c) increases with the incorporation of the passivation layer, which leads to deeper perovskite VBMs. The highest VBM shift is observed for the TPPSe passivated sample, followed by the TPPS and TPPO passivated films (Figure 3.d). The change in the UPS spectra of the perovskite is related to the donation of electrons from the Lewis base, which is also confirmed through the DFT calculations. The strong VBM shift for the TPPSe is indicative of its soft Lewis base properties. The observed trend is similar to the one observed for the NiO VBM position (Figure S.4).[22] When comparing the VBM position for the NiO and perovskite films (Figure 3.b-d and S.4) it is observed that with the addition of the passivators, the interfacial VBM alignment becomes more favorable, which might improve interfacial charge transfer. Among all four conditions, pristine NiO-perovskite shows the

poorest band alignment. In contrast, alignment improves gradually from TPPO to TPPS to TPPSe, and eventually, TPPSe shows the best interfacial VBM alignment. Though the VBM alignment for NiO, TPPO, and TPPS in Figure S.4.d may appear sub-optimal for interfacial charge transfer, Dänekamp et al. showed that slight interfacial band misalignment might not significantly affect the device PCE.[23] Nonetheless, a suitable band alignment is desirable for the most optimal interfacial charge transfer.

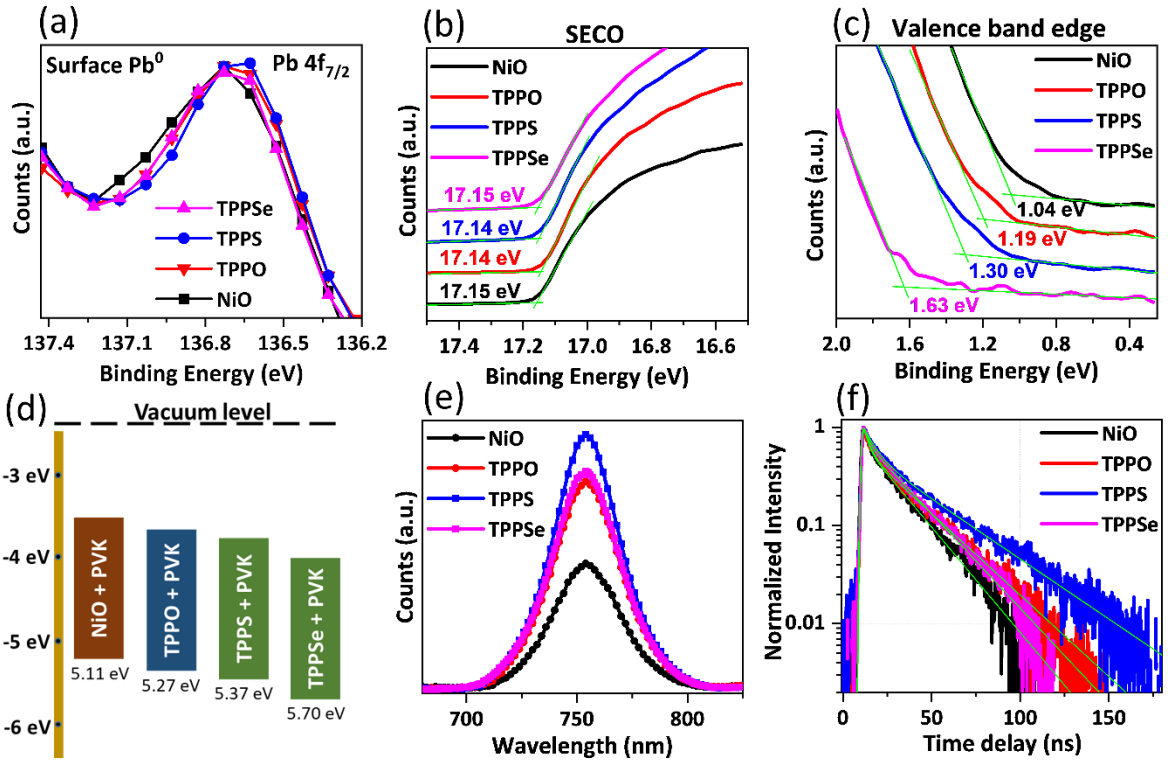

Figure 3. (a) XPS of the Pb $4f_{7/2}$ (Pb^0) peak from the surface of the perovskite film with and without the passivation layers. The exact peak locations can be seen in Table S.4. (b) The secondary electron cut-off (SECO), (c) Valence band edge from the UPS of the surface of the perovskite films with different interface passivators. (d) Perovskite (PVK) VBM position with/without interface passivators in the NiO-perovskite interface. (e) Steady-state photoluminescence of the perovskite films; (f) Normalized TRPL kinetics of the perovskite films without or with the passivation layers, extracted at 740−770 nm window and excited with 600 nm pulses at a fluence of 3.5 μJ cm^{-2}.

The surface SEM images show that the grain size of the perovskite films remains the same across the passivated and non-passivated samples (Figure S.12), indicating that the passivation molecules do not have a significant impact on perovskite crystal nucleation and growth. The absorbance pattern of the films (Figure S.13.a) also shows no noticeable change, indicating consistent film thickness and composition. The calculated band gap of the perovskite film is 1.62 eV. Additionally, XRD data (Figure S.13.b) confirms that the passivation molecules have a negligible effect on film crystallinity, as evidenced by similar diffractograms across all four samples. These results demonstrate that interface passivations have minimal impact on the bulk properties of the perovskite film.

PL intensity and its corresponding change are often employed as an indicator to assess the film and interface quality as well as device efficiency. The photoluminescence (PL) spectra (Figure 3.e) are recorded for the four perovskite films coated on top of the NiO HTL layer. The maximum PL increase is observed with the TPPS passivated film, followed by the TPPSe and TPPO passivated ones. To gain further insight into the carrier recombination behavior of the perovskite films, time-resolved photoluminescence (TRPL) study has been carried out. The passivated films exhibit 'long tails' in their pseudo-color TRPL plots relative to the control film, indicating longer PL lifetimes (Figure S.14). A more distinct comparison of TRPL kinetics is illustrated in Figure 3.f. Considering trap-assisted nonradiative recombination and electron-hole radiative recombination mechanisms in perovskites, the kinetics were fitted with a simplified biexponential equation $I(t) = A_1\exp(-t/\tau_1) + A_2\exp(-t/\tau_2)$ (Table S.5), where τ_1 and τ_2 denote short and long lifetimes, respectively. In comparison with the control perovskite, a significant increase of both τ_1 and τ_2 is observed for all the passivated films. To accurately comprehend PL and TRPL results, it is critical to interpret them in relation to interfacial charge transfer and radiative recombination characteristics within an absorber film. Figure S.4.d demonstrates that TPPSe shows the most optimal band alignment (with perovskite), while

pristine NiO shows the least favorable band alignments. The superior band alignment due to the interface passivators is expected to lead to PL quenching in the perovskite film. However, contrary to the expectation, an increase in the PL intensity after the incorporation of the passivation molecules is observed. We believe this is the result of two competing phenomena: (a) PL quenching due to the improved band alignment and (b) PL enhancement due to interfacial trap passivation (reduced SRH recombination). An overall increase in the absolute PL intensity upon the addition of the interface passivators indicates that the second phenomenon is the dominant one. This indicates that our passivating agents possess strong trap passivation capabilities, which outweigh the PL quenching effects caused by their superior band alignment. The higher PL intensity and longer carrier lifetime for the TPPS passivated film compared to the TPPO passivated sample is indicative of its superior ability to passivate interface defects, thus suppressing the nonradiative recombination at the interface. A moderate increase (compared to TPPS) in the PL and TRPL for the TPPSe sample is due to its applied lower solution concentration than the other two passivators. The PL and TRPL lifetime closely resemble the peak shift trend observed in the Pb^0 4f XPS spectra, indicating that the Pb-X (X=O, S, Se) interaction strength has a vital role in the trap passivation mechanism.

The performance of the four types of devices is compared in Figures 4.a-b, S.15-16, and the corresponding device parameters are summarized in Table S.6. All three passivators improve the PCE and V_{OC} of the devices compared to the control devices. TPPO and TPPS-based devices show the maximum improvement in the device PCE. This improvement in PCE can be linked to the effective trap passivation by TPPO and TPPS, whose effect is also observed in the PL and TRPL characterizations. Some of the improvement in the PCE can also be due to the role of passivating molecules in changing the band alignment at the NiO-perovskite interface, as discussed earlier. The TPPSe passivated device is slightly inferior to the former two, possibly due to its lower concentration and the formation of secondary phases at the

interface, as discussed earlier. Figure S.16 shows the hysteresis of the J-V graph for all four samples. All the graphs show a small amount of hysteresis. However, no statistically significant change in the hysteresis index could be detected after the incorporation of the interface passivations. The incident photon-to-current efficiency (IPCE) spectra for all four devices (Figure 4.c) exhibit a similar trend to the J_{SC} results obtained from the J-V curves. After incorporating passivation layers, there is a slight improvement in quantum efficiency, mainly in the lower wavelength section of the IPCE graph. This is because higher energy photons with lower wavelengths are absorbed near the bottom interface of the solar cell. With the passivation layers, recombination at the bottom interface is suppressed, resulting in a higher IPCE in that region. We acknowledge that the PCE reported in this work is comparatively lower than some of the other reports in the literature. However, we believe that the comparative evaluation of different interface passivators should not be influenced by the overall optimization or baseline PCE of the device. Nonetheless, the device performance of this work can be further improved by utilizing thermally evaporated PCBM & BCP, passivation of the top interface (perovskite-ETL) with SAM molecules/ 2D perovskite, and by using more efficient organic HTLs like PTAA as the bottom transport layer.

Figure S.17.a shows the semi-log dark J-V graph of the perovskite solar cell devices. It can be seen that the un-passivated NiO device shows the highest amount of leakage current. On the other hand, the TPPS passivated device shows the lowest amount of leakage current, whereas TPPO and TPPSe-based devices show a moderate amount of leakage current. The leakage current in the device has been linked to reduced shunt resistance and increased SRH-recombination, which in turn can be linked to the trap density inside the device.[24] In order to measure the trap density inside our perovskite devices, hole-only devices with an FTO/NiO/Perovskite/Spiro-OMeTAD/Au structure were fabricated (Figure S.17.b-f). The current-voltage response of the hole-only device was measured in dark conditions.[25] The hole-

only device shows three distinct regions in its J-V graph: at a lower voltage, it shows ohmic response; at moderate voltage, it shows trap-filled limit (TFL) characteristics; whereas at a higher voltage, it shows space-charge-limited current (SCLC) characteristics.[26] In order to measure the trap density, the inflection point between the ohmic and trap-filled regions (V_{TFL}) is determined. To calculate the trap density, the following equation is used:

$$N_{trap} = \frac{2\varepsilon\varepsilon_0 V_{TFL}}{eL^2} \quad \ldots\ldots\ldots\ldots\ldots\ldots\ldots\ldots (1)$$

where, ϵ_0 is the vacuum permittivity, ϵ is the relative dielectric constant of perovskite (ϵ = 32), e is the elementary charge of the electron, V_{TFL} is trap-filled limit voltage, N_{trap} is the trap-state density inside the device, L is the thickness of the perovskite film (500 nm).[27] The derived trap density values for NiO, TPPO, TPPS, and TPPSe are 2.19 X 10^{15}, 1.67 X 10^{15}, 1.44 X 10^{15}, and 1.63 X 10^{15} $cm^{-3,}$ respectively. The TPPO, TPPS, and TPPSe treatment causes a 24%, 34%, and 26% reduction in the overall trap density compared to the control sample. Additionally, it should be considered that these results demonstrate an overall reduction in trap density. Since we anticipate most of this reduction to occur at the interface, the actual percentage of trap density reduction at the interface is likely even higher.

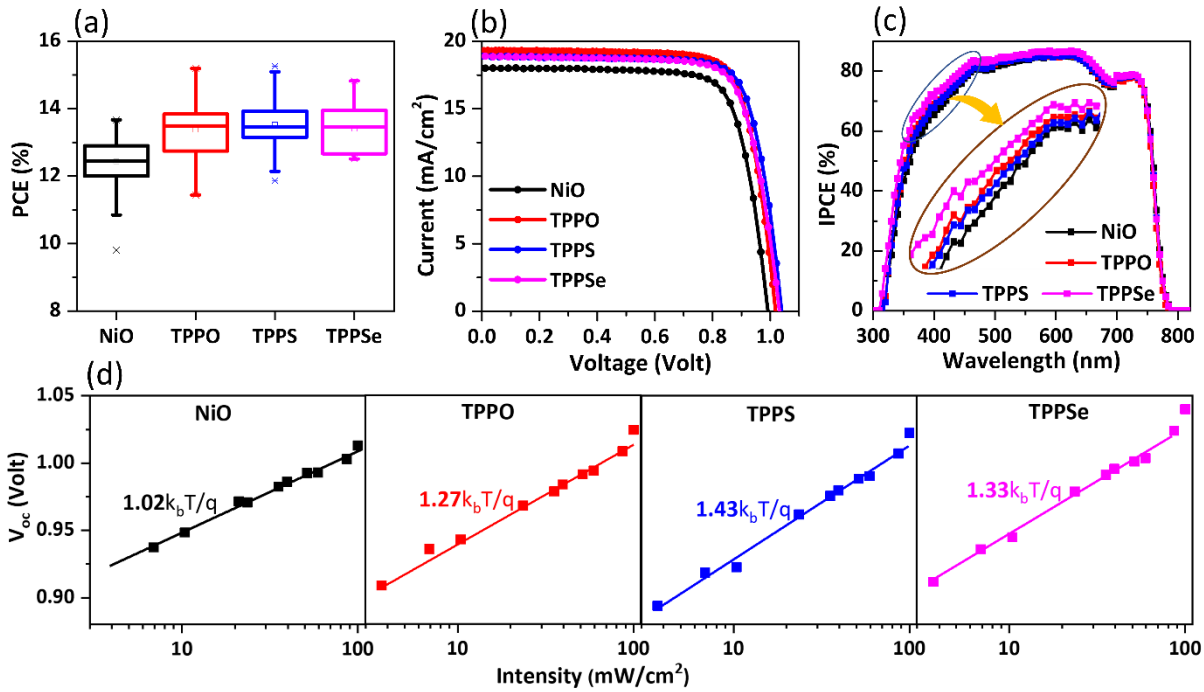

Figure 4. (a) Statistical power conversion efficiency (PCE) data of the control (NiO), TPPO, TPPS, and TPPSe passivated perovskite solar cells, the statistical graph of the J_{SC}, $V_{OC,}$ and Fill factor are in the supporting information (Figure S.15). (b) *J-V* curve of the best-performing devices for all four types of samples (Table S.6, Figure S.16) (c) IPCE graph of perovskite solar cell devices with and without the interface passivators. (d) Light intensity vs. V_{OC} graph for the control and TPPO, TPPS, and TPPSe passivated solar cell devices, the ideality factor values of all four samples are also shown inside the graph.

Figure 4.d plots V_{OC} as a function of illumination intensity (from 1 sun to 0.05 sun) for the NiO, TPPO, TPPS, and TPPSe devices. The ideality factor (n_{id}) is calculated from the slope of the light intensity vs. V_{OC} graph using the following formula:

$$n_{id} = \frac{q}{k_b T}\frac{dV_{OC}}{dI} \ldots\ldots\ldots\ldots\ldots\ldots (2)$$

where, V_{OC} is the open circuit voltage at a particular light intensity, k_b is the Boltzmann constant, T is the temperature, q is the elementary charge, and I is illumination intensity.[28] The extracted ideality factor is 1.02, 1.27, 1.43, and 1.33 for NiO, TPPO, TPPS, and TPPSe

devices, respectively. It is commonly accepted that an ideality factor close to 1 is correlated with higher radiative recombination behavior and better device performance. However, other issues like first-order interfacial SRH recombination can also give an ideality factor close to 1 due to electron-hole density imbalance in the interface, leading to an erroneous interpretation of the diode quality.[29] P Caprioglio et al. demonstrated that even in a superior-quality halide perovskite film, the fraction of radiative recombination (measured via photoluminescence quantum yield) is too low to generate an ideality factor close to 1.[30] They argue that, generally, perovskite solar cells should have an ideality factor close to 2, and only the presence of dominating interfacial recombination will cause the value to approach 1. The low ideality factor of the NiO-based devices is possibly due to the existence of severe interfacial recombination. The incorporation of the passivation molecules reduces interfacial defect density, leading to lower interfacial monomolecular recombinations and a higher ideality factor value.[31] The highest degree of passivation is observed for the TPPS, followed by TPPSe and TPPO, which is highly correlated with the trap density trend observed in the hole-only device.

Figure 5.a shows the stability of the perovskite devices when stored at 40% relative humidity (RH) and ambient temperature (20 °C). The NiO and TPPO-based devices lose close to 50% of their initial PCE after 600 hours, whereas in the same timeframe, TPPS and TPPSe-passivated devices retain 71% and 74% of their initial PCEs. T_{75}, the time taken to reach 75% of the initial efficiency, is calculated using the linear interpolation method. The T_{75} value for NiO, TPPO, TPPS, and TPPSe is determined to be 393, 417, 510, and 589 hours respectively. To measure the maximum power point (MPP) stability, the power output of the unencapsulated devices is measured under continuous 1 sun illumination in the presence of 80% RH (Figure 5.b). Though no additional heat source is provided, due to the effect of the constant illumination, the device temperature is recorded to reach up to 50 °C. After 12 hours, TPPS

and TPPSe passivated devices retained 93% and 94% of their initial PCE, while their bare NiO and TPPO-based counterparts retained only 78% and 86% of their initial PCE, respectively.

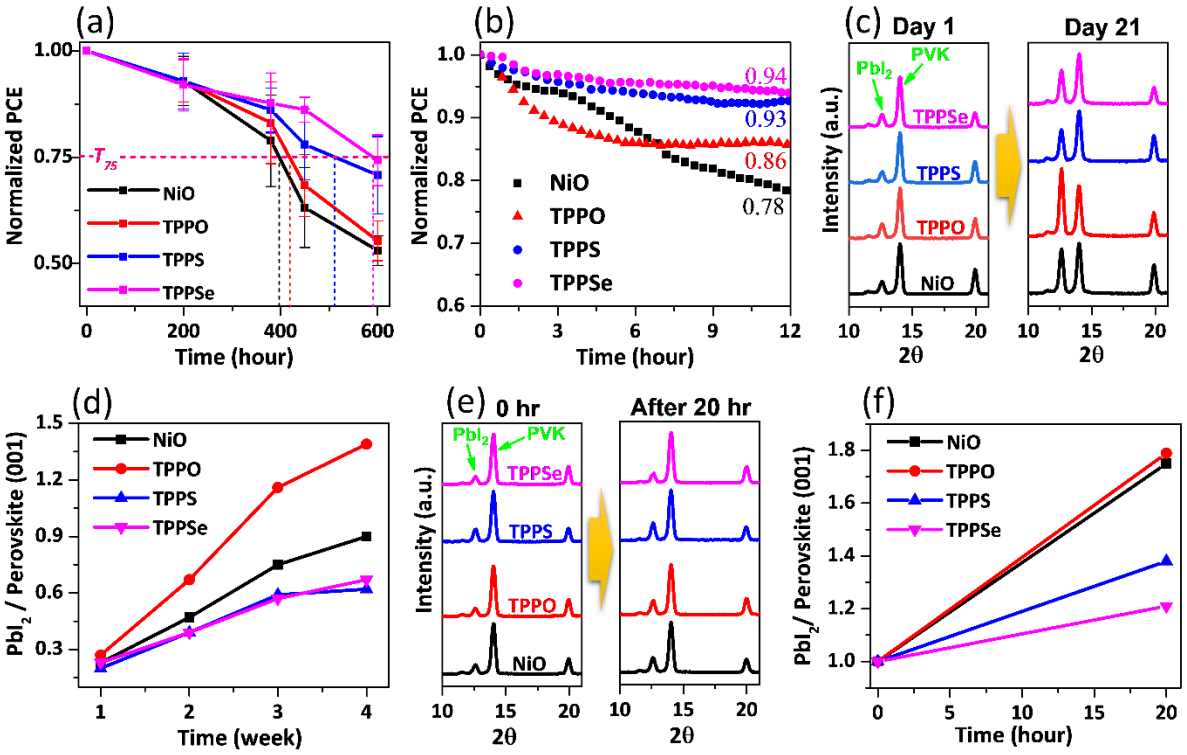

Figure 5. (a) Ambient stability of the perovskite solar cell devices. The stability is measured under the presence of 40% RH and 20 °C ambient temperature. The T_{75} line shows the point at which the devices retain 75% of their initial PCE. (b) Maximum power point (MPP) PCE of the devices. This PCE is measured under continuous 1 sun illumination in the presence of 80% RH. (c) XRD of the perovskite film & (d) The change in the PbI_2-perovskite (001) peak intensity ratio over time, with different interface passivators, before and after aging at 40% RH and 20 °C. (e) XRD of the perovskite film & (f) The change in the PbI_2-perovskite (001) peak intensity ratio over time, the samples are exposed to continuous 1 sun illumination under the presence of 80% RH.

To better understand the underlying reason behind the improved stability of the TPPS and TPPSe passivated devices, the degradation behavior of the unencapsulated perovskite films is studied. The ambient stability of the films is assessed by performing XRD characterization on the fresh films and aged films that are stored in the dark at 40% RH and ambient temperature

(20 °C). Figures 5.c. 5.d & S.18 show the change in the PbI_2 (001)-perovskite (110) peak intensity ratio with time. The increase in structural disorder and the formation of additional PbI_2 phase, both indicative of the degradation in the perovskite film, increases the ratio. Even though the PbI_2 increase is observed for all four samples, the increase is significantly higher in the NiO and TPPO passivated samples compared to the TPPS and TPPSe passivated ones. To monitor the combined effect of light and humidity on the degradation behavior of the perovskite films, the devices are subjected to continuous 1-sun illumination at 85% RH for 20 hours (Figures 5.e, 5.f & S.19). The XRD diffractograms taken from the films before and after the exposure show that the increase in the PbI_2/perovskite peak ratio is substantially lower for the TPPS and TPPSe passivated films as compared to the NiO and TPPO passivated ones. In the MPP device stability study (Figure 5.b), the TPPO passivated devices show an unusually rapid degradation at the initial phase of the study, which eventually reaches a saturation point. To gain insight into this phenomenon, we analyzed the XRD results shown in Figure S.19, conducted under similar illumination conditions. It is observed that after 20 hours of aging under 1 sun illumination, TPPO passivated devices show a significantly higher amount of phase segregation than the other three samples (Figure S.20), which might be responsible for the rapid degradation in its device PCE. However, the PCE degradation stopped once the phase segregation reached a saturation point. Due to trap passivation in TPPO, the degradation after the initial fast decay phase is significantly suppressed compared to the pristine NiO sample. The occurrence of phase segregation is frequently linked to the presence of light, making it a probable explanation for its observation in the MPP stability study but its absence in our ambient stability study (Figure 5.a).[32]. Nonetheless, though it is interesting that TPPO can facilitate phase segregation inside the perovskite film, the actual mechanism is unclear at this moment.

Previous studies have shown that Pb-related defects, such as under-coordinated Pb atoms and Pb^0 defect clusters, can cause severe degradation and increased nonradiative recombination in perovskite solar cells. [19, 33]The reduction in PbI_2 formation observed in TPPS and TPPSe samples may be attributed to their strong interaction with Pb^{2+} and Pb^0-related defects (Figure 1.c and 3.a). This interaction effectively passivates the defects, diminishing their active role in the degradation process and resulting in an increased energetic barrier for the degradation reaction.[4b] The strong defect passivation ability of TPPS (and TPPSe) is supported by its lower trap density, higher PL, higher carrier lifetime, and higher ideality factor. Despite the superior defect passivation, the PCE of TPPS-passivated devices does not show significant improvement compared to TPPO-passivated devices. This could be due to the neutralization of shallow defects by TPPS, which does not affect the PCE. S Tan et al. showed that shallow defects, which are ubiquitous inside the perovskite lattice, are considered to have minimal impact on the PCE but can still strongly affect the stability of the devices.[4b]

In addition to passivating different point defects through chemical interaction, an effective defect passivator should also be able to maintain the passivation in the presence of various environmental stressors. The stronger interaction strength between the Pb and the S/Se atoms, as shown in our DFT calculations, allows the dative bonds (Pb-S/Se) to withstand the attack of moisture and temperature more effectively, further improving the stability of the devices (Figure 1.c). This is likely the reason for the superior stability of TPPSe-passivated devices, despite having similar PL and ideality factors compared to TPPO-passivated devices. However, the effectiveness of the TPPSe molecule in this work is not optimum due to the formation of secondary phases in the NiO-perovskite interface. Therefore, in the future, other types of transport layers will be explored where this issue can be avoided. Nevertheless, even with a smaller concentration, TPPSe still shows comparable, if not higher, stability with the TPPS-passivated devices. If the use of Se-based molecules is not restricted by other secondary factors

due to their higher softness, they could significantly outcompete oxygen and sulfur-based defect passivators in terms of stability in perovskite solar cells. Our DFT calculation also supports this hypothesis which shows that TPPSe has 30% higher binding energy compared to TPPO and 7.5% higher binding energy than TPPS. Therefore, further investigation and exploration are needed to provide valuable insights into the efficacy of Se-based compounds in improving the stability and performance of perovskite solar cells in the future.

3. Conclusions:

This study investigates the efficacy of three different chalcogenide-based interface passivators, TPPO, TPPS, and TPPSe, in enhancing the stability and PCE of perovskite solar cells. The study finds that all three passivators improve the device PCE to a comparable extent due to the superior band alignment and improved recombination characteristics in the interface. The findings also reveal that the TPPS and TPPSe passivated devices showed significantly better stability than control and TPPO passivated devices. This is attributed to the stronger interaction of TPPS and TPPSe with Pb ions, particularly Pb^0-related defects, due to a better softness match between the defects and the passivator molecules. Based on our DFT calculations, selenium shows the strongest binding with the Pb-based defects, making selenium-based compounds very promising for interface passivator applications. The higher binding energy (confirmed by DFT) allows TPPS and TPPSe to effectively passivate interfacial and bulk traps, validated through photoluminescence, trap density measurement, and ideality factor characterizations. Additionally, these stronger Pb-S or Pb-Se interactions enable these dative bonds to better withstand external stressors, such as heat, moisture, and photons, further enhancing the device stability.

From this study, two main conclusions can be drawn: first, sulfur and selenium-based passivators are effective in passivating Pb-related cation defects, and second, matching the softness (or hardness) of the defects and passivator molecules is crucial for effective defect passivation. While the author acknowledges that softness is not the only parameter determining the defect passivation ability of a molecule, it provides valuable insight into the defect passivation mechanism in the perovskite lattice. This study provides a better understanding of defect passivation inside the perovskite lattice and provides valuable insight for selecting more effective passivation molecules.

4. Experimental:

4.1. Materials

All the chemicals and reagents are used as received from chemical companies. Lead iodide (PbI2, 99.99%) and lead bromide ($PbBr_2$, >98%), cesium iodide (99.999%), isopropanol (99.5%), chlorobenzene (99.8%) and dimethylformamide (99.8%), dimethyl sulfoxide (99.9%), triphenylphosphine oxide (98%), nickel(II) acetate tetrahydrate (>98%), ethanolamine (>99%), 2-Methoxyethanol (>99.8%) are purchased from Sigma-Aldrich. Methylammonium bromide (MABr, >99.99%) and formamidinium iodide (FAI, >99.99%) are purchased from GreatCell Solar. [6,6]-phenyl-C61-butyric acid methyl ester (PC61BM, 99.5%), Spiro-MeOTAD (99.5%) are purchased from Lumtec Corp. Triphenylphosphine sulfide (>99%), and triphenylphosphine selenide (>98%) are purchased from Tokyo Chemical Industry Co., Ltd. The chemicals were directly used without going through any further purifications.

4.2. Solution preparation:

For preparing the NiO precursor solution, 0.2 mM of Ni-acetate and 0.2 mM of ethanolamine are added to 1 ml of 2-methoxy ethanol. The solution is then transferred into a hotplate and heated to 70 ℃ for 1 hour. After one hour, a clear green color solution is formed, which is cooled down and later used for the spin coating.

For preparing the perovskite precursor solution, 0.2 mM MABr, 1 mM FAI, 1.1 mM PbI_2, and 0.22 mM of $PbBr_2$ are dissolved in 1 ml of the solvent containing DMF and DMSO in the ratio of 4:1. The mixture is heated to 70 ℃ until a clear and homogeneous solution formed. To complete the precursor solution synthesis, 42.2 µl of 1.5 molar CsI solution (in DMSO) is added to the previously prepared perovskite precursor solution. The solution is heated for another 30 minutes at 70 ℃ to form a homogeneous solution.

To prepare the Spiro-OMeTAD solution, 50 mg of Spiro-MeOTAD is dissolved in 700 µl of chlorobenzene, and then 20 µl of 4-tertbutylpyridine is added to the solution. For doping purposes, 12.4 µL of a Li salt solution (consisting of 26 mg of lithium bis-(trifluoromethylsulfonyl)imide in 50 µl of acetonitrile) is added. The entire solution is then stirred for 15 minutes at 70°C.

TPPO, TPPS, and TPPSe precursor solutions of different concentrations are prepared inside the glovebox by dissolving the respective compounds in the desired concentration (as described earlier) in isopropanol. The solution mixture is placed in a hotplate at a temperature of 60℃ for a few hours until it forms a clear homogeneous solution.

4.3. Device fabrication:

The perovskite solar cell is fabricated on the FTO substrate. FTO substrates are partially etched using HCl and Zn powder to make room for the top electrode deposition. The etched FTO substrates are cleaned in soap water and ethanol bath subsequently. After that, the air-dried FTO substrates are treated in a UV-ozone chamber to make their surface hydrophilic. The cleaned FTO substrates are coated with the previously prepared nickel oxide precursor solution using the spin coating method with a spin speed of 3000 rpm for 30 seconds. To complete the deposition of the NiO film, it is annealed at 400 ℃ for 1 hour.

After annealing, the films are instantly transferred into the glovebox, where the passivation layers are deposited. TPPO, TPPS, and TPPSe films are deposited on top of the NiO film using spin coating at a spin rate of 4000 rpm for 30 seconds. After the deposition, the films are dried at room temperature for one hour before proceeding to the next step. After that, the perovskite layer is deposited using an antisolvent-assisted two-step spin coating method. In the first step, the spin speed is set at 1000 rpm for 10 seconds to facilitate the proper spreading of the solution;

in the second step, the film is spun at the speed of 6000 rpm for 30 seconds. Five seconds before the spinning finished, 120 µl of antisolvent (chlorobenzene) is dropped into the rotating substrate. After that, the film is transferred to a preheated hotplate and is annealed at 105 ℃ for 30 minutes. A 20 mg/ml PCBM solution in chlorobenzene is used to deposit the electron transport layer. PCBM deposition is completed at a spin speed of 2000 rpm for 30 seconds, followed by an annealing step at 90 ℃ for 10 minutes. For depositing the buffer layer, a 0.5 mg/ml bathocuproine solution (in isopropanol) is spin-coated at 5000 rpm for 30 seconds. After that, the devices are stored in the glovebox for 48 hours before depositing the electrode. Finally, a 100 nm thick silver layer is thermally evaporated to complete the device. For the fabrication of the hole-only device, the fabrication method was similar up to the perovskite deposition layer. After that, the Spiro-OMeTAD solution is spin-coated at a spin speed of 4000 rpm for 30 seconds on top of the perovskite layer. Finally, a 70 nm thick Au electrode is deposited using thermal evaporation.

4.4. Characterization and measurements:

UV-vis spectroscopy is carried out by using UV-3600 (Shimadzu) spectrophotometer. For XRD characterization, Bruker D8 Advance diffractometer is used. The XRD of the perovskite film is completed by using standard gonio scan mode. X-ray Photoelectron Spectroscopy (XPS) and Ultraviolet photoelectron spectroscopy (UPS) are carried out by using the AXIS Supra XPS instrument (Kratos Analytical Ltd, UK). For carrying out the bulk XPS and UPS, 40-50% thickness is etched using Ar+ ions. Photoluminescence characterization is performed by using Fluorolog, FL-1057, Horiba Instruments equipped with 450 W Xe Lamp. PL spectra from the perovskite are obtained by using a 600 nm excitation wavelength. The transient photoluminescence (TRPL) measurements were conducted using an Optronis Optoscope streak camera system with the sample excited by 600 nm femtosecond laser excitation (3.5 µJ cm^{-2}),

which was generated from a Coherent Astrella femtosecond laser system (50 fs, 1 kHz, 800 nm) with Topas Prime collinear optical parametric amplifiers (OPAs). Note that all the TRPL samples were excited at the sample surface side. *J-V* measurements are carried out by XES-40S2-CE (San-El Electronic Co., Ltd) solar simulator and Keithley 2401 source meter. The calibration of the light intensity is done by using a standard silicon solar cell from Newport. SEM images are acquired by using ZEISS Field Emission Scanning Electron Microscope. For measuring the ambient device stability, devices are stored in a controlled dry box with 40% RH and 20°C temperature. For carrying out the stability of the devices under the light, they are illuminated with 1 sun illumination in the presence of 80% relative humidity. The current output is measured using a voltage that is 10 mV lower than MPP voltage point to eliminate the effect of fluctuation of the MPP point. For measuring the film stability under light, they are exposed to the same 1 sun illumination and 80% RH.

4.5. DFT Calculations

First-principles calculations are carried out using density functional theory (DFT) within the VASP code.[34] The frozen-core projected augmented wave approach is employed to account for electron and core interactions.[35] The Perdew–Burke–Ernzerhof (PBE) generalized gradient approximation is utilized for the exchange-correlation functional.[36] The kinetic energy cutoff for the plane-wave basis functions is set to 400 eV. Brillouin zone integration is performed using k-point meshes with grid spacings of $2\pi \times 0.025$ Å^{-1} or smaller. To simulate the PbI_2-terminated (001) surface of the α-$FAPbI_3$ phase, a $2 \times 2 \times 1$ supercell slab with five atomic layers is constructed.[37] The surface is fully relaxed until the total energies converge to 10^{-4} eV. Van der Waals interactions are considered in all the DFT calculations.

4.6. Statistics

For preparing Figure S.2, 24 devices for TPPO, 24 devices for TPPS and 40 devices for TPPSe were fabricated (2 device per substrate). For preparing the Figure 4.a and S.15 data from 96 devices were collected (2 device per substrate and average 24 devices for each conditions). For producing Figure 5.a, 34 devices were fabricated. Parameters were analyzed using originPro (2016) software.

Supporting Information

Supporting Information is available from the Wiley Online Library or from the author.

Conflicts of interest

There are no conflicts to declare.

Acknowledgements

This work was supported by the Singapore Ministry of Education (MOE) Tier 2 grant (MOE T2EP50120-0008). This research is funded by the National Research Foundation, Prime Minister's Office, Singapore under its Campus for Research Excellence and Technological Enterprise (CREATE) program. We would like to acknowledge the Facility for Analysis, Characterization, Testing and Simulation, Nanyang Technological University, Singapore, for use of their XPS/UPS facilities. The photophysics studies were supported by the grants funded by the Singapore Ministry of Education under its AcRF Tier 2 grant (MOE-T2EP50120-0004) and the NRF under NRF Investigatorship (NRF-NRFI-2018-04).

References

[1] a) NREL, Best Research-Cell Efficiency Chart, https://www.nrel.gov/pv/cell-efficiency.html, accessed; b) J. Park, J. Kim, H.-S. Yun, M. J. Paik, E. Noh, H. J. Mun, M. G. Kim, T. J. Shin, S. I. Seok, *Nature* **2023**, DOI: 10.1038/s41586-023-05825-y.

[2] T.-B. Song, Q. Chen, H. Zhou, C. Jiang, H.-H. Wang, Y. Yang, Y. Liu, J. You, Y. Yang, *J. Mater. Chem. A* **2015**, 3, 9032.

[3] J. Bisquert, E. J. Juarez-Perez, *The Journal of Physical Chemistry Letters* **2019**, 10, 5889.

[4] a) L. K. Ono, S. Liu, Y. Qi, *Angewandte Chemie International Edition* **2020**, 59, 6676; b) S. Tan, I. Yavuz, M. H. Weber, T. Huang, C.-H. Chen, R. Wang, H.-C. Wang, J. H. Ko, S. Nuryyeva, J. Xue, Y. Zhao, K.-H. Wei, J.-W. Lee, Y. Yang, *Joule* **2020**, 4, 2426.

[5] K. Liu, S. Dai, F. Meng, J. Shi, Y. Li, J. Wu, Q. Meng, X. Zhan, *J. Mater. Chem. A* **2017**, 5, 21414.

[6] H. Xie, Z. Wang, Z. Chen, C. Pereyra, M. Pols, K. Gałkowski, M. Anaya, S. Fu, X. Jia, P. Tang, D. J. Kubicki, A. Agarwalla, H.-S. Kim, D. Prochowicz, X. Borrisé, M. Bonn, C. Bao, X. Sun, S. M. Zakeeruddin, L. Emsley, J. Arbiol, F. Gao, F. Fu, H. I. Wang, K.-J. Tielrooij, S. D. Stranks, S. Tao, M. Grätzel, A. Hagfeldt, M. Lira-Cantu, *Joule* **2021**, 5, 1246.

[7] a) D. P. Nenon, K. Pressler, J. Kang, B. A. Koscher, J. H. Olshansky, W. T. Osowiecki, M. A. Koc, L.-W. Wang, A. P. Alivisatos, *Journal of the American Chemical Society* **2018**, 140, 17760; b) Y. Bai, H. Chen, S. Xiao, Q. Xue, T. Zhang, Z. Zhu, Q. Li, C. Hu, Y. Yang, Z. Hu, F. Huang, K. S. Wong, H.-L. Yip, S. Yang, *Adv. Funct. Mater.* **2016**, 26, 2950; c) Z. Wang, A. Pradhan, M. A. kamarudin, M. Pandey, S. S. Pandey, P. Zhang, C. h. Ng, A. S. M. Tripathi, T. Ma, S. Hayase, *ACS Appl. Mater. Interfaces* **2019**, 11, 10012; d) S. R. Wang, A. L. Wang, X. Y. Deng, L. S. Xie, A. D. Xiao, C. B. Li, Y. Xiang, T. S. Li, L. M. Ding, F. Hao, *J. Mater. Chem. A* **2020**, 8, 12201; e) A. Sadhu, M. Rai, T. Salim, X. Jin, J. M. R. Tan, S. W. Leow, M. G. Ahmed, S. Magdassi, S. G. Mhaisalkar, L. H. Wong, *Adv. Funct. Mater.* **2021**, 31, 2103807.

[8] a) J. C. Hamill, Jr., O. Romiluyi, S. A. Thomas, J. Cetola, J. Schwartz, M. F. Toney, P. Clancy, Y.-L. Loo, *The Journal of Physical Chemistry C* **2020**, 124, 14496; b) L. F. Zhu, Y. Z. Xu, P. P. Zhang, J. J. Shi, Y. H. Zhao, H. Y. Zhang, J. H. Wu, Y. H. Luo, D. M. Li, Q. B. Meng, *J. Mater. Chem. A* **2017**, 5, 20874; c) G. Giorgi, K. Yamashita, H. Segawa, *Physical Chemistry Chemical Physics* **2018**, 20, 11183.

[9] R. G. Pearson, *Journal of Chemical Education* **1968**, 45, 581.

[10] S. Ahrland, presented at Structure and Bonding, Berlin, Heidelberg, 1968//, **1968**.

[11] a) R. G. Pearson, *Inorganic Chemistry* **1988**, 27, 734; b) R. A. Kerner, T. H. Schloemer, P. Schulz, J. J. Berry, J. Schwartz, A. Sellinger, B. P. Rand, *Journal of Materials Chemistry C* **2019**, 7, 5251.

[12] a) I. Wharf, T. Gramstad, R. Makhija, M. Onyszchuk, *Canadian Journal of Chemistry* **1976**, 54, 3430; b) in *Lewis Basicity and Affinity Scales*, DOI: https://doi.org/10.1002/9780470681909.ch1 **2009**, p. 1.

[13] T. Pan, W. Zhou, Q. Wei, Z. Peng, H. Wang, X. Jiang, Z. Zang, H. Li, D. Yu, Q. Zhou, M. Pan, W. Zhou, Z. Ning, *Advanced Materials* **2023**, 35, 2208522.

[14] a) S. Ding, M. Hao, C. Fu, T. Lin, A. Baktash, P. Chen, D. He, C. Zhang, W. Chen, A. K. Whittaker, Y. Bai, L. Wang, *Advanced Science* **2022**, 9, 2204476; b) J. Haruyama, K. Sodeyama, L. Han, Y. Tateyama, *The Journal of Physical Chemistry Letters* **2014**, 5, 2903; c) C. Li, X. Wang, E. Bi, F. Jiang, S. M. Park, Y. Li, L. Chen, Z. Wang, L. Zeng, H. Chen, Y. Liu, C. R. Grice, A. Abudulimu, J. Chung, Y. Xian, T. Zhu, H. Lai, B. Chen, R. J. Ellingson, F. Fu, D. S. Ginger, Z. Song, E. H. Sargent, Y. Yan, *Science* **2023**, 379, 690.

[15] a) J. He, Y. Xiang, F. Zhang, J. Lian, R. Hu, P. Zeng, J. Song, J. Qu, *Nano Energy* **2018**, 45, 471; b) Q. Wang, C.-C. Chueh, T. Zhao, J. Cheng, M. Eslamian, W. C. H. Choy, A. K.-Y. Jen, *ChemSusChem* **2017**, 10, 3794; c) P. Ru, E. Bi, Y. Zhang, Y. Wang, W. Kong, Y. Sha, W. Tang, P. Zhang, Y. Wu, W. Chen, X. Yang, H. Chen, L. Han, *Advanced Energy Materials* **2020**, 10, 1903487.

[16] J. Chang, Y.-C. Wang, C. Song, L. Zhu, Q. Guo, J. Fang, *Journal of Materials Chemistry C* **2018**, 6, 6982.

[17] B. Tu, Y. Shao, W. Chen, Y. Wu, X. Li, Y. He, J. Li, F. Liu, Z. Zhang, Y. Lin, X. Lan, L. Xu, X. Shi, A. M. C. Ng, H. Li, L. W. Chung, A. B. Djurišić, Z. He, *Advanced Materials* **2019**, 31, 1805944.

[18] a) S. P. Dunfield, L. Bliss, F. Zhang, J. M. Luther, K. Zhu, M. F. A. M. van Hest, M. O. Reese, J. J. Berry, *Advanced Energy Materials* **2020**, 10, 1904054; b) Z. Wang, M. A. Kamarudin, N. C. Huey, F. Yang, M. Pandey, G. Kapil, T. L. Ma, S. Hayase, *ChemSusChem* **2018**, 11, 3941.

[19] a) J. Liang, X. Hu, C. Wang, C. Liang, C. Chen, M. Xiao, J. Li, C. Tao, G. Xing, R. Yu, W. Ke, G. Fang, *Joule* **2022**, 6, 816; b) A. Kirakosyan, N. D. Chinh, M. R. Sihn, M.-G. Jeon, J.-R. Jeong, D. Kim, J. H. Jang, J. Choi, *The Journal of Physical Chemistry Letters* **2019**, 10, 4222.

[20] *Journal of the American Chemical Society* **2002**, 124, 1830.

[21] R. Wang, J. Xue, K.-L. Wang, Z.-K. Wang, Y. Luo, D. Fenning, G. Xu, S. Nuryyeva, T. Huang, Y. Zhao, J. L. Yang, J. Zhu, M. Wang, S. Tan, I. Yavuz, K. N. Houk, Y. Yang, *Science* **2019**, 366, 1509.

[22] E. M. Miller, Y. X. Zhao, C. C. Mercado, S. K. Saha, J. M. Luther, K. Zhu, V. Stevanovic, C. L. Perkins, J. van de Lagemaat, *Physical Chemistry Chemical Physics* **2014**, 16, 22122.

[23] B. Danekamp, N. Droseros, D. Tsokkou, V. Brehm, P. P. Boix, M. Sessolo, N. Banerji, H. J. Bolink, *Journal of Materials Chemistry C* **2019**, 7, 523.

[24] K. Tvingstedt, L. Gil-Escrig, C. Momblona, P. Rieder, D. Kiermasch, M. Sessolo, A. Baumann, H. J. Bolink, V. Dyakonov, *ACS Energy Letters* **2017**, 2, 424.

[25] Y. Zhang, P. Wang, M.-C. Tang, D. Barrit, W. Ke, J. Liu, T. Luo, Y. Liu, T. Niu, D.-M. Smilgies, Z. Yang, Z. Liu, S. Jin, M. G. Kanatzidis, A. Amassian, S. F. Liu, K. Zhao, *Journal of the American Chemical Society* **2019**, 141, 2684.

[26] C. Liu, J. Tu, X. Hu, Z. Huang, X. Meng, J. Yang, X. Duan, L. Tan, Z. Li, Y. Chen, *Adv. Funct. Mater.* **2019**, 29, 1808059.

[27] Q. Dong, Y. Fang, Y. Shao, P. Mulligan, J. Qiu, L. Cao, J. Huang, *Science* **2015**, 347, 967.

[28] N. E. Courtier, *Physical Review Applied* **2020**, 14, 024031.

[29] P. Calado, D. Burkitt, J. H. Yao, J. Troughton, T. M. Watson, M. J. Carnie, A. M. Telford, B. C. O'Regan, J. Nelson, P. R. Barnes, *Physical Review Applied* **2019**, 11.

[30] P. Caprioglio, C. M. Wolff, O. J. Sandberg, A. Armin, B. Rech, S. Albrecht, D. Neher, M. Stolterfoht, *Advanced Energy Materials* **2020**, 10.

[31] a) Y. Kumar, E. Regalado-Perez, J. J. Jerónimo-Rendón, X. Mathew, *Solar Energy Materials and Solar Cells* **2022**, 236, 111512; b) Z. Zhang, Z. Li, L. Deng, Y. Gao, C. Wang, J. Xu, T. Li, P. Gao, *ACS Appl. Mater. Interfaces* **2022**, 14, 4378.

[32] D. J. Slotcavage, H. I. Karunadasa, M. D. McGehee, *ACS Energy Letters* **2016**, 1, 1199.

[33] a) S. G. Motti, D. Meggiolaro, A. J. Barker, E. Mosconi, C. A. R. Perini, J. M. Ball, M. Gandini, M. Kim, F. De Angelis, A. Petrozza, *Nature Photonics* **2019**, 13, 532; b) L. Wang, H. Zhou, J. Hu, B. Huang, M. Sun, B. Dong, G. Zheng, Y. Huang, Y. Chen, L. Li, Z. Xu, N. Li, Z. Liu, Q. Chen, L.-D. Sun, C.-H. Yan, *Science* **2019**, 363, 265; c) A. Alberti, C. Bongiorno, E. Smecca, I. Deretzis, A. La Magna, C. Spinella, *Nature Communications* **2019**, 10, 2196.

[34] G. Kresse, J. Furthmüller, *Physical Review B* **1996**, 54, 11169.

[35] G. Kresse, D. Joubert, *Physical Review B* **1999**, 59, 1758.

[36] J. P. Perdew, K. Burke, M. Ernzerhof, *Physical Review Letters* **1996**, 77, 3865.

[37] H. Chen, H. Yan, Y. Cai, *Chem. Mat.* **2022**, 34, 1020.

The table of contents

In this work, the interface passivation capability of different chalcogenide-based molecules has been investigated. It is observed that compared to oxygen-based passivators, the sulfur and selenium-based molecules are more effective in passivating the interfacial defects and enhancing the stability of perovskite solar cells.

*Anupam Sadhu, Yuanyuan Guo, Teddy Salim, Qingde Sun, Subodh G. Mhaisalkar, Tze Chien Sum, Lydia H. Wong**

Elucidating the role of chalcogenide-based interface passivators in enhancing the stability of perovskite solar cells

TOC figure